ADVANCED SCIENCE Open Access
www.advancedscience.com

Proton-Coupled Electron Transfer on $Cu_2O/Ti_3C_2T_x$ MXene for Propane (C_3H_8) Synthesis from Electrochemical CO_2 Reduction

Jun Young Kim, Won Tae Hong, Thi Kim Cuong Phu, Seong Chan Cho, Byeongkyu Kim, Unbeom Baeck, Hyung-Suk Oh, Jai Hyun Koh, Xu Yu, Chang Hyuck Choi, Jongwook Park, Sang Uck Lee,* Chan-Hwa Chung, and Jung Kyu Kim**

Electrochemical CO_2 reduction reaction (CO_2RR) to produce value-added multi-carbon chemicals has been an appealing approach to achieving environmentally friendly carbon neutrality in recent years. Despite extensive research focusing on the use of CO_2 to produce high-value chemicals like high-energy-density hydrocarbons, there have been few reports on the production of propane (C_3H_8), which requires carbon chain elongation and protonation. A rationally designed 0D/2D hybrid Cu_2O anchored-$Ti_3C_2T_x$ MXene catalyst (Cu_2O/MXene) is demonstrated with efficient CO_2RR activity in an aqueous electrolyte to produce C_3H_8. As a result, a significantly high Faradaic efficiency (FE) of 3.3% is achieved for the synthesis of C_3H_8 via the CO_2RR with Cu_2O/MXene, which is ≈26 times higher than that of Cu/MXene prepared by the same hydrothermal process without NH_4OH solution. Based on in-situ attenuated total reflection-Fourier transform infrared spectroscopy (ATR-FTIR) and density functional theory (DFT) calculations, it is proposed that the significant electrocatalytic conversion originated from the synergistic behavior of the Cu_2O nanoparticles, which bound the $*C_2$ intermediates, and the MXene that bound the *CO coupling to the C_3 intermediate. The results disclose that the rationally designed MXene-based hybrid catalyst facilitates multi-carbon coupling as well as protonation, thereby manipulating the CO_2RR pathway.

1. Introduction

With the continuously increasing demand to reduce CO_2 emissions, the conversion of CO_2 into value-added hydrocarbon products has gained significant attention.[1] From an energy perspective, utilization of CO_2 to produce high-value chemicals, particularly those with high energy density, such as hydrocarbons with long carbon chains or saturated (i.e., hydrogen-rich) hydrocarbons, is desirable. In particular, propane (C_3H_8) has a high specific energy (50.4 MJ kg^{-1}) with a remarkably low global warming potential (< 1) compared to other CO_2-driven products including CO, CH_4, and C_2H_4, thereby considered a desirable renewable energy source to reduce the impact on carbon footprint with versatile applications.[2] Among the various technologies to utilize CO_2 to produce C_3H_8, the electrochemical conversion of CO_2 can be effective since the electrochemical CO_2 reduction reaction (CO_2RR) operates under environmentally benign mild conditions, using renewable electricity. However, the electrochemical

J. Y. Kim, W. T. Hong, T. K. C. Phu, S. C. Cho, B. Kim, U. Baeck, S. U. Lee, C.-H. Chung, J. K. Kim
School of Chemical Engineering
Sungkyunkwan University (SKKU)
2066, Seobu-ro, Jangan-gu, Suwon 16419, Republic of Korea
E-mail: suleechem@skku.edu; legkim@skku.edu

H.-S. Oh, J. H. Koh
Clean Energy Research Center
Korea Institute of Science and Technology (KIST)
Hwarang-ro 14-gil 5, Seongbuk-gu, Seoul 02792, Republic of Korea

X. Yu
School of Chemistry and Chemical Engineering
Yangzhou University
Yangzhou 225002, P. R. China

C. H. Choi
Department of Chemistry
Pohang University of Science and Technology (POSTECH)
Pohang 37673, Republic of Korea

The ORCID identification number(s) for the author(s) of this article can be found under https://doi.org/10.1002/advs.202405154

DOI: 10.1002/advs.202405154

CO_2RR to C_3H_8 in an aqueous electrolyte is challenging because the reaction involves several steps, including carbon chain elongation and protonation with 20 electrons. Thus, modulating the electrochemical catalysts to promote the protonation of longer-chain carbons is critical to produce C_3H_8. To the best of our knowledge, few studies report a notable Faradaic efficiency for C_3H_8 of the electrochemical CO_2RR in an aqueous electrolyte, but most of the research achieved a modest Faraday efficiency (FE) of ≈1%, without the aid of other ionomers or carbon sources.[3]

A recent study with imidazolium-functionalized Mo_3P coated with the ionomer (ImF-Mo_3P) showed FE of 91% C_3H_8, marking a significant advance over previous reports that typically showed FE less than 1% or even trace amounts.[4] However, the carbon sources, i.e., carbon functional groups, namely imidazolium moieties on the catalyst, as well as the coated ionomers, are participating in the CO_2RR.[5] These carbon sources inhibit the identification of the reaction mechanism to find the crucial $*C_2$ and $*C_3$ intermediates for C_3H_8. Especially, *in-situ* Raman data pinpointing appropriate CO_2RR intermediates other than *CO to support the proposed reaction mechanism from CO_2 to C_3H_8 is required. Given that the *CO formation is an initial step of CO_2RR, peaks for *CO alone cannot directly substantiate the C_3H_8 production. Thus, a rational strategy by facilitating multi-carbon coupling and protonation supported by substantial experimental evidence to represent the reaction mechanism is required.

Cu-based catalyst is generally considered to produce multiple hydrocarbons of various chain lengths from CO_2.[6] Some studies on Cu-based catalysts reported a wide selectivity for C_3 products including n-propanol, acetone, and hydroxyacetone,[7] albeit the FE of C_3H_8 is generally less than 0.3%, or even a traceable amount, indicating a lack of protonation.[8] To increase the selectivity toward multi-carbon, Zhang et al. reported that not only the electron transfer for CO dimerization at catalytic active sites but also several protonation steps are necessary.[9]

$Ti_3C_2T_x$ MXene with 2D layered structure has received considerable attention due to its catalytic performance in the electrochemical CO_2RR with excellent chemical durability and abundant adsorption sites with tunable functional groups on the surface.[10] Especially, in an aqueous electrolyte, the naturally modulated O- and OH- functional group of MXene can share H with CO_2RR intermediates, enabling proton-coupled electron transfer (PCET) for the protonation of hydrocarbon products, thus increasing the energy density of CO_2 reduction products.[11]

C. H. Choi
Institute of Convergence Research and Education in Advanced Technology (I-CREATE)
Yonsei University
Seoul 03722, Republic of Korea
J. Park
Integrated Engineering
Department of Chemical Engineering
Kyung Hee University
Gyeonggi 17104, South Korea
E-mail: jongpark@khu.ac.kr
J. K. Kim
SKKU Advanced Institute of Nano Technology (SAINT)
Sungkyunkwan University
2066 Seobu-ro, Suwon 16419, Republic of Korea

Besides, modulating the MXene functional groups with O- or OH- can result in high chemical reactivity and an increase in the number of active sites for catalytic reactions in an aqueous electrolyte.[12] Thus, the composite of Cu_2O and MXene can be useful for hydrocarbon generation with long-term stability, given that the modulated MXene surfaces and oxygen-derived Cu offer stable adsorption sites for CO_2 molecules, further promoting C-C coupling and effective protonation of longer-chain hydrocarbons.[11,13]

In this study, we designed a rational hybrid structure of Cu_2O incorporated into MXene (Cu_2O/MXene) for the efficient conversion of CO_2 into multi-carbon products, especially C_3H_8 which requires C_3 coupling and sufficient protonation. To understand the synergistic effect of the Cu_2O and MXene with the mechanism of CO_2 conversion to C_3H_8, Cu_2O/MXene was characterized by X-ray photoelectron spectroscopy (XPS), Fourier-transform infrared spectroscopy (FT-IR), Auger electron spectroscopy (AES) and X-ray absorption spectroscopy (XAS). Notably, attenuated total reflection-Fourier transform infrared spectroscopy (ATR-FTIR) revealed that the interfacial effect between Cu_2O and MXene was significant for $*C_2$–$*C_1$ coupling. Specifically, Cu_2O strongly bound and preserved $*C_2$ intermediates. In contrast, the MXene bound to the sole $*C_1$ site and provided sufficient protons to the CO_2RR intermediates. As a result, Cu_2O/MXene reveals an efficient C_3H_8 production with a FE of 3.3% at −1.3 V versus reversible hydrogen electrode (RHE) in CO_2 saturated 0.1 M $KHCO_3$, without the aid of carbon sources. We envision that our strategy of catalyst design combined with Cu_2O and MXene, which could tune the selectivity toward multi-carbon products and proton-coupled electron transfer, respectively, is able to produce saturated hydrocarbon products with high energy density, such as C_3H_8.

2. Results

2.1. Characterizations for Cu_2O/MXene

Cu_2O/MXene was fabricated via a facile hydrothermal process. First, $Ti_3C_2T_x$ MXene nanosheets were prepared by a selective Al etching method, starting from Ti_3AlC_2 MAX powder with further delamination, following the previous study with some modifications.[14] Cu nanoparticles (CuNPs) were prepared separately by the hot-injection method. After individually fabricating MXene and CuNPs, the mixture solution of MXene and CuNPs was transferred to a Teflon liner, with 4 mmol NH_4OH solution added to adjust pH ≈10, and autoclaved for 30 min at 70 °C. During the synthesis, some of the functional groups of the MXene nanosheets were modulated to hydroxyl (-OH) moieties in the presence of an NH_4OH solution. In addition, the NH_4OH solution induced partial oxidation of CuNPs to form Cu_2O and further consolidated Cu_2O on the MXene. The as-prepared samples were then freeze-dried to prevent further oxidation and restacking. To compare the CO_2RR activity, Cu/MXene was synthesized in the same manner as Cu_2O/MXene without the use of an NH_4OH solution, so the CuNPs were not significantly oxidized when anchored to MXene during the synthesis.

Transmission electron microscopy (TEM) was used to examine the structural morphology of Cu_2O/MXene (**Figure 1**). As shown in Figure 1a-b, the Cu NPs adhered to the MXene nanosheets.

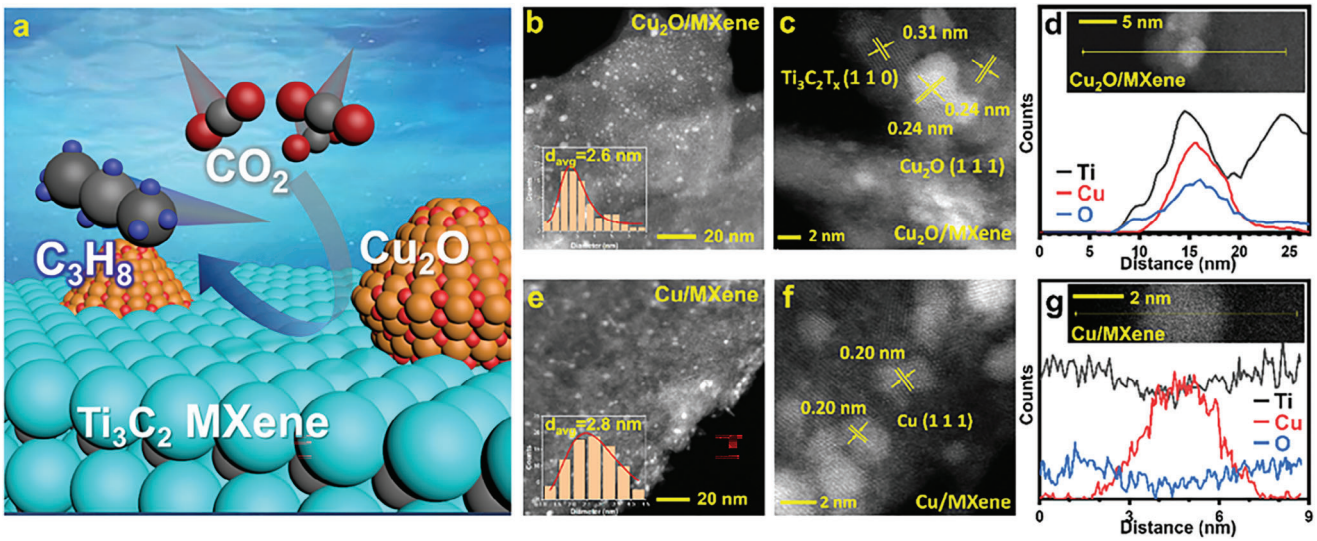

Figure 1. a) Schematic illustration of CO_2RR with Cu_2O/MXene. TEM, HRTEM, and EDS line profile mapping for b–d) Cu_2O/MXene and e–g) Cu/MXene. b) and e) TEM images of Cu_2O/MXene and Cu/MXene. c) and f) HRTEM for Cu_2O/MXene and Cu/MXene. d) and g) EDS line profile mapping Ti, Cu, and O for Cu_2O/MXene and Cu/MXene.

As shown in Figure 1b, the CuNPs were distributed on the surface of MXene with 2.6 nm of average diameter, showing a typical log-normal distribution. The high-resolution TEM (HRTEM) image in Figure 1c shows that the CuNPs in Cu_2O/MXene were crystalline structures with lattice fringes of 0.24 nm for Cu_2O (111). This indicates the partial oxidation of CuNPs during the hydrothermal process in the presence of NH_4OH solution to form Cu_2O. However, no morphological variance was observed between MXene and NH_4OH-treated MXene (AT-MXene), as shown in Figure S1 (Supporting Information). In addition, a clear interface was observed between the CuNPs and MXene. EDS line profile scanning was conducted to assign Ti (black), Cu (red), and O (blue) (Figure 1d,g), where a clear interface between the CuNPs and MXene was observed. The elemental O distribution was higher in the presence of Cu, indicating the incorporation of CuNPs as Cu_2O phase into MXene.

As for the Cu/MXene, which was synthesized without NH_4OH treatment, the average diameter of the CuNPs on Cu/MXene was 2.8 nm with a narrower size distribution compared to Cu_2O/MXene (Figure 1e). In addition, the CuNPs in Cu/MXene, which predominantly presents a lattice fringe with 0.20 nm for Cu (111), are metallic Cu (Figure 1f). In Figure 1g, metallic CuNPs are observed with no change in the elemental O distribution, whereas an increase in the Ti content is observed in Cu/MXene. Thus, the presence of NH_4OH during the synthesis induced the incorporation of CuNPs being transformed to Cu_2O on the surface of the MXene nanosheets.

Following up on the TEM results, electron energy-loss spectrometry (EELS) was performed to determine the valence states of the Cu species in Cu_2O/MXene and Cu/MXene (**Figure 2a**). From the EELS spectra, the slope for Cu_2O/MXene in the range of 930–940 eV was between those of Cu and Cu_2O, but close to that of Cu_2O. Therefore, it was difficult to distinguish the valence state of Cu in Cu/MXene from that in Cu_2O/MXene. These results may imply that the valence state of Cu in both Cu_2O/MXene and Cu/MXene was a combination of metallic Cu and Cu^+. Additionally, by comparing the EELS spectra of Cu_2O/MXene and Cu/MXene in the range of 400–750 eV, representing MXene, we found a low residual F intensity with a higher O intensity in Cu_2O/MXene (Figure S2, Supporting Information). This indicates that the NH_4OH treatment induced not only the partial oxidation of CuNPs but also the successful functional group modulation of MXene in Cu_2O/MXene during the hydrothermal process.

The crystal and phase structures of Cu_2O/MXene were characterized by XRD (Figure 2b). The two distinct main peaks (i.e., (002) and (004)) represent MXene, which is consistent with the results of previous studies.[15] The (002) peak at 8.87° is a typical peak for the $Ti_3C_2T_x$ MXene, indicating a c-lattice parameter (c-LP, ≈ 19.9 Å).[16] This (002) peak did not shift in Cu/MXene. However, the (002) peak shifted toward a lower value (7.06°) in Cu_2O/MXene with c-LP to 25.0 Å when Cu_2O was anchored to the MXene. This result may imply that the CuNPs were anchored to the functional group of MXene as Cu_2O phase, affecting the lattice structure and eventually increasing the interlayer distance of MXene.[17] In Cu_2O/MXene, the composition of Cu_2O (111) was higher than the Cu (111) (JCPDS 77–0199 and JCPDS 04–0836, respectively). The ratio from the quantitative phase analysis by Rietveld refinement for Cu:Cu_2O was 0.17:0.83, indicating a high fraction of Cu_2O. A sharp peak with low intensity for Cu_2O (111) was also observed for Cu/MXene. Unlike Cu_2O/MXene, the ratio of Cu:Cu_2O in Cu/MXene was 0.91:0.09, indicating that most of the CuNPs were composed of Cu^0. Thus, NH_4OH treatment affected the oxidation state of Cu in Cu_2O/MXene.

FT-IR was conducted to determine the chemical bonds and functional groups on the surface of Cu_2O/MXene. As shown in Figure 2c, the peak at 540 cm^{-1} is attributed to the vibration of the Ti-O bond from the MXene.[18] Cu-O stretching vibration peaks are also observed at 425 cm^{-1} and 620 cm^{-1},[19] presumably the CuNPs were hybridized onto the -O or -OH functional group of MXene forming Cu_2O. The broad absorption band with a peak at 3445 cm^{-1} corresponds to the -OH stretching

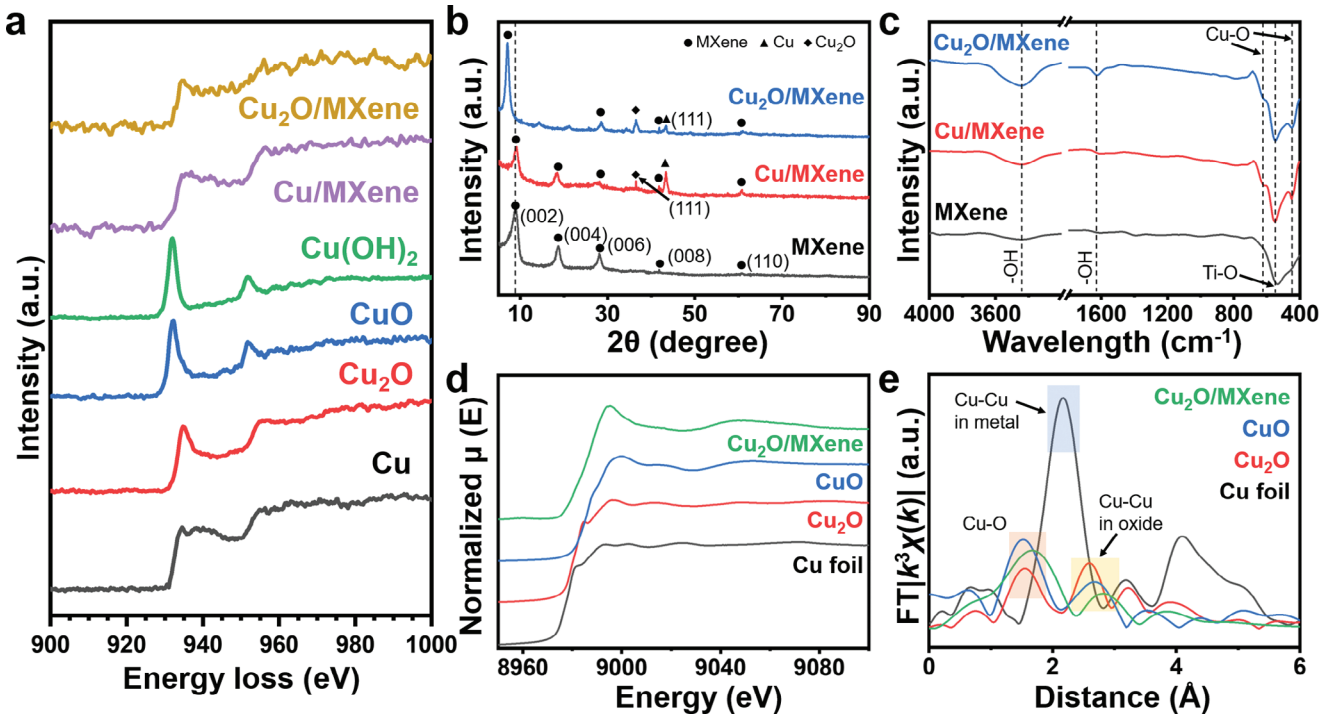

Figure 2. a) EELS spectra of Cu/MXene and Cu_2O/MXene. b) XRD and c) FT-IR spectra of MXene, Cu/MXene and Cu_2O/MXene. d) XANES and e) FT-EXAFS data for Cu_2O/MXene.

vibration of the water molecules in the MXene interlayer.[20] For the Cu_2O/MXene where NH_4OH treatment was applied, the FT-IR spectra showed a slight peak at 1625 cm^{-1} which is attributed to the OH groups.[21] Thus, this result suggests that the NH_4OH treatment modulated the functional group of the MXene to the -OH.

The coordination environment of the CuNPs in Cu_2O/MXene was further characterized by synchrotron-based X-ray absorption near-edge structure (XANES) and extended X-ray absorption fine structure (EXAFS). As shown in Figure 2d, the Cu absorption edge of Cu_2O/MXene resided between those of commercial Cu and Cu_2O. Especially, the Cu k-edge for Cu_2O/MXene was in between those of Cu_2O and CuO but close to that of Cu_2O, suggesting that the average oxidation state of Cu is likely to be higher than that of Cu^+ but lower than that of Cu^{2+}. This valence state also reflected the successful hybridization of Cu_2O and MXene, where Cu_2O was anchored to MXene. The Fourier transform (FT)-EXAFS spectra of Cu_2O/MXene and the references (Figure 2e) showed the intensity of the Cu-O peak at ≈1.6 Å, which was intermediate between the intensities found in Cu_2O and CuO. The increase in Cu-O distance on Cu_2O/MXene also shows evidence of Cu-O-Ti bonding by hybridization, as the length of the Cu-O bond from the Cu-O-Cu is shorter than the Cu-O-Ti bond length.[22] The Cu-Cu peak from the oxide (≈2.8 Å) is distinct in Cu_2O/MXene which is associated with the scattering path of the second Ti shell (i.e., Ti L-shell).[22]

XPS was further performed to elucidate the chemical structure of Cu_2O anchored to MXene from Cu_2O/MXene, compared with MXene and Cu/MXene (**Figure 3**). In the XPS high-resolution spectra of C 1s (Figure 3a), the binding energy peak at 284.8 eV was assigned to the adventitious carbon of C-C.[20] Furthermore, the binding energy of C-Ti in Cu_2O/MXene shifted to a lower value (282.3 eV) than that of bare MXene (282.6 eV), indicating that Cu_2O transferred electrons to MXene. The oxygen contents with carbon (C-O, C = O, and O-C = O) peaks may result from MXene oxidation and carbon networks.[23] In the XPS Ti 2p spectra (Figure 3b), the binding energies of Ti-C, Ti^{2+}, Ti^{3+}, and Ti^{4+} for MXene are 455.4, 456.1, 457.3, and 458.8 eV, respectively. Specifically, the Ti^{2+}, Ti^{3+}, and Ti^{4+} peaks are attributed to Ti-X, Ti-O, and Ti-O_x (including Ti-$(OH)_x$), respectively.[24] When CuNPs are hybridized onto the MXene (Cu/MXene and Cu_2O/MXene), the CuNPs are consolidated at the oxygen-rich functional group of MXene. The evidence of anchoring CuNPs on MXene is further characterized by the O 1s XPS. The O 1s region of the MXene was deconvoluted by components corresponding to C-Ti-O_x, Ti-O-Ti, C-Ti-$(OH)_x$, O_{ads} at BE = 530.5, 531.2, 532.0, and 533.2 eV, respectively (Figure 3c).[25] O_{ads} is the surface adsorbed oxygen species in MXene, and the peak at BE = 533.2 eV corresponds to adsorbed water.[26] The peak for the adsorbed water was significantly increased when Cu_2O was applied to the MXene, affecting the hydrophilicity. In addition, compared to the MXene, Cu/MXene and Cu_2O/MXene display a positive shift of C-Ti-O_x and Ti-O-Ti, demonstrating that the CuNPs were anchored onto the MXene terminals. Notably, the N 1s peak in AT-MXene or Cu_2O/MXene was not observed, indicating that the NH_4OH treatment affected the functional group modulation of MXene to the -OH group and did not participate in the N-doped or amine groups (Figure S7, Supporting Information). Besides, as MXene was fabricated and stored as a solution, the MXene already has some -OH functional groups, even without NH_4OH treatment. Thus, the NH_4OH treatment slightly increased the number of -OH functional groups. The result is in accordance

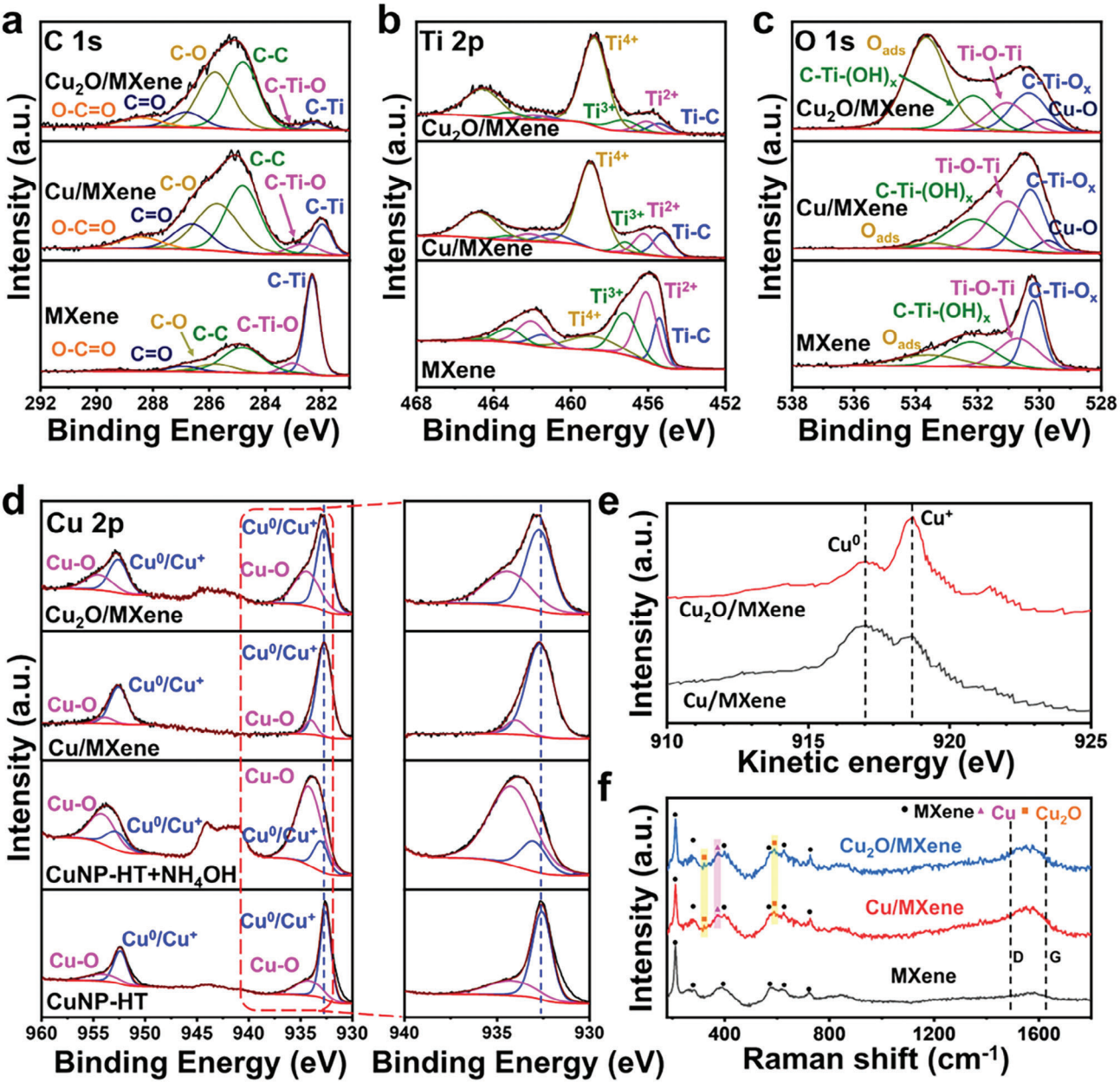

Figure 3. XPS spectra of a) C 1s, b) O 1s, and c) Ti 2p of MXene, Cu/MXene and Cu_2O/MXene. d) Cu 2p of Cu/MXene and Cu_2O/MXene displayed with a magnified view of XPS Cu $2p_{3/2}$ comparing with CuNP prepared with hydrothermal process in the presence and absence of NH_4OH treatment. e) Cu LMM AES spectra of Cu/MXene and Cu_2O/MXene. f) Raman spectra of MXene, Cu/MXene, and Cu_2O/MXene.

with the previous research by Gogotsi's group, which modulated the MXene functional group by the NH_4OH solution to the -OH.[27]

To determine the valence state of Cu, the Cu 2p XPS for Cu_2O/MXene was compared with that of Cu/MXene, as well as CuNPs with the hydrothermal process (CuNP-HT) in the absence and presence of NH_4OH treatment (Figure 3d). The Cu^0/Cu^+ and Cu^{2+} peaks of Cu $2p_{3/2}$ were observed at 933.0 and 934.2 eV. Without MXene, the NH_4OH solution easily oxidized the surface of CuNP to form Cu_2O or even further oxidized to CuO. Thus, a significant increase in the Cu^{2+} peak was observed compared with CuNP-HT and Cu_2O (CuNP-HT+NH_4OH). The typical Cu^{2+} satellites at 940–945 eV and 960–965 eV also confirmed the further oxidation of Cu to CuO with NH_4OH treatment in the absence of MXene, in accordance with the XRD data (Figure S3, Supporting Information).[28] In the presence of MXene, although the Cu^0/Cu^+ peak was shifted to a higher binding energy, NH_4OH treatment cannot fully oxidize Cu to Cu^{2+} since NH_4OH also affects the partial substitution of the functional group of MXene to -OH. Cu LMM Auger electron spectra (AES) were tested to further carefully distinguish the oxidation state of the CuNPs decorated on MXene (Figure 3e). Comparing the

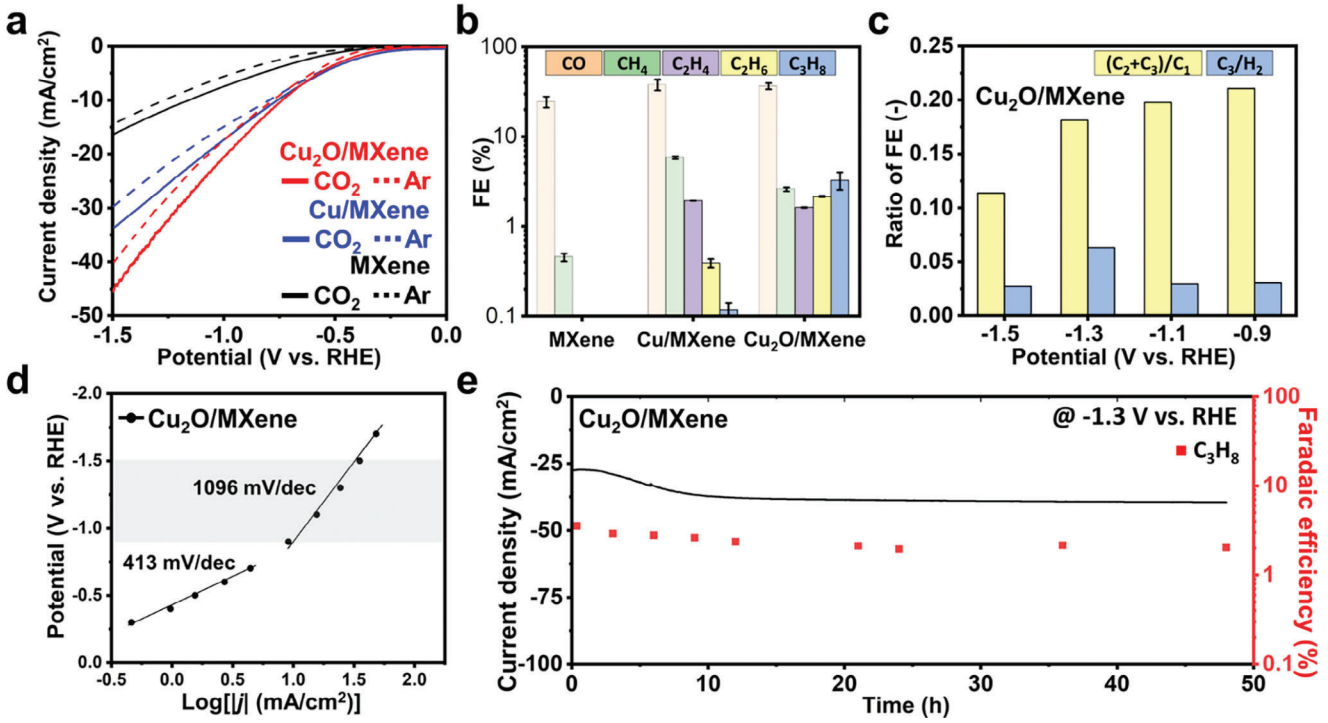

Figure 4. Electrochemical tests of Cu_2O/MXene. a) LSV curves of Cu/MXene and Cu_2O/MXene saturated with CO_2 (straight lines) and Ar (dashed lines). Applied potential is corrected with iR compensation, and ECSA is considered for current density. b) Faradaic efficiency on each carbonaceous CO_2RR product at −1.3 V versus RHE. Error bars represent the standard deviation in FE calculated after three tests for repeatability. The other non-carbon product is listed in Table S2 (Supporting Information). c) Relative ratio of the FE with Cu_2O/MXene. d) Tafel slope with Cu_2O/MXene. The intermediate overpotential region where significant C_3 production was detected is highlighted in grey. e) Stability tests of Cu_2O/MXene at −1.3 V versus RHE.

intensities of Cu^0 and Cu^+, Cu^+ was dominant in Cu_2O/MXene, whereas Cu^0 was dominant in Cu/MXene.

The chemical structure of Cu_2O/MXene was revealed using Raman spectroscopy (Figure 3f). Signals representing the vibrations of Ti and C atoms were observed in MXene, Cu/MXene, and Cu_2O/MXene (i.e., peaks at 201, 274, 386, 582, 626, and 726 cm^{-1}).[10] The peak located at 201 cm^{-1} is attributed to the out-of-plane vibrations of Ti atoms, whereas the peaks at 274 and 386 cm^{-1} are ascribed to the in-plane vibrations of the surface groups attached to the Ti atoms.[29] The two peaks at 1373 cm^{-1} and 1576 cm^{-1} represent the D band and G band, respectively, where the former D-band is generally related to the disordered graphite formed by defects in carbon-based materials, whereas the latter G-band is ascribed to the stacking of the graphite hexagonal network plane.[10,15a] For Cu/MXene and Cu_2O/MXene, both Cu and Cu_2O were observed (376 cm^{-1} for Cu, and 322 and 590 cm^{-1} for Cu_2O, respectively).[30] Thus, Cu could be slightly oxidized when anchored to MXene, even when the NH_4OH treatment was not applied to Cu/MXene.

2.2. Electrochemical Analysis for CO_2 Reduction

Linear sweep voltammetry (LSV) curves in Ar and CO_2 saturated electrolyte were used to evaluate the CO_2RR performance of Cu_2O/MXene, and then the results were compared with those of MXene and Cu/MXene (**Figure** 4a). MXene, Cu/MXene, and Cu_2O/MXene showed activity on CO_2RR. Anchoring Cu_2O on MXene further increased the activities of both CO_2RR and hydrogen evolution reaction (HER), according to the results obtained with CO_2 and Ar saturation. The current density of Cu_2O/MXene in CO_2 purged electrolyte was higher than that in the Ar, demonstrating its good electrocatalytic activity for CO_2 reduction. In addition, the CO_2 saturated LSV curves for all samples exhibited more positive onset potentials than the Ar-saturated ones, suggesting that their activities on CO_2 participated in the reaction. Note that these current density data can be enhanced with different cell configuration such as a membrane electrode assembly (MEA) cell. The electrochemical impedance spectroscopy (EIS) was conducted to investigate the kinetic behaviors of the electrocatalyst for CO_2RR in CO_2-saturated 0.1 M $KHCO_3$ (Figure S9, Supporting Information). For the Cu NPs showed low charge transfer resistance reflecting efficient CO_2RR activity in high frequency region but extremely large diffusion resistance in low frequency region. In cases of MXene and AT-MXene, both exhibited large semi-circles which indicate insufficient CO_2RR, which are coherent to the product analysis. The Cu/MXene showed smaller semi-circle than those of MXene and AT-MXene by enhanced charge transfer due to the Cu anchoring. Especially, the Cu_2O/MXene displayed the lowest charge transfer resistance among the MXene-based electrocatalysts reflecting superior activity for CO_2RR. From the CO_2RR, products with CO, CH_4, C_2H_4, C_2H_6, and C_3H_8 were observed. The FEs of the CO_2RR products at the applied potentials for MXene, AT-MXene,

Cu/MXene, and Cu_2O/MXene are shown in Figure S13 (Supporting Information). As shown in Figure S14 (Supporting Information), the GC-FID chromatograms clearly confirm that the gaseous product is comprised with CH_4, C_2H_4, and C_3H_8, not including C_3H_6. The FE of the CO_2RR products on Cu_2O/MXene at −1.3 V versus RHE was compared with that of Cu/MXene in Figure 4b, where the highest FE_{C3H8} was observed. Cu_2O/MXene was the most active electrocatalyst, affording 3.3% of FE_{C3H8} at −1.3 V versus RHE as the optimum potential, suggesting effective electron and proton transfer during CO_2 reduction. These results were comparable to those obtained for Cu/MXene with ≈0.1% FE_{C3H8}. Although MXene also exhibited activity in CO_2, the products of the CO_2RR were C_1 gases composed of CO and CH_4. Especially, as the major products of Cu or Cu_2O are C_1 and C_2 products,[31] the presence of MXene in the composite may affect the C_3 intermediate production toward C_3H_8. We also compared the experimental C_2 & C_3 to C_1 ratio with −0.9 to −1.5 V versus RHE, as shown in Figure 4c. When the applied potential increased, the $(C_2+C_3)/C_1$ ratio decreased, indicating that the time for carbon coupling became insufficient as the HER is significantly affected by the higher applied potential, which is the competitive reaction of CO_2RR. Additionally, the FE of both CO and CH_4 decreased with increasing applied potential (Figure S13, Supporting Information), indicating that the HER favored over the CO_2RR.[7a] An interesting result on the ratio of C_3 to H_2 was found at −1.3 V versus RHE, showing the highest value. In general, the C_3/H_2 ratio is low as *H adsorption onto the catalyst during the HER requires less energy than the protonation of the hydrocarbon products.[3b] However, as the MXene could provide protons to the C_3 intermediate, the highest C_3H_8 FE at −1.3 V versus RHE could be achieved by a proton-coupled electron-transfer step, while concurrently reducing the HER.[11]

Generally, selectivity is highly dependent on the competitive adsorption of intermediates such as *CO and *OCCO, as well as the reaction kinetic energy barrier of the rate-determining step in the electrochemical CO_2RR for C_3H_8 production.[32] The Tafel plot was tested for Cu_2O/MXene and Cu/MXene, highlighting the CO_2RR intermediate overpotential region (−0.9 to −1.5 V versus RHE) where significant C_3 products were observed (Figure 4d; Figure S15, Supporting Information). The Tafel slope of the Cu/MXene at −0.9 to −1.5 V versus RHE was 957 mV dec^{-1}, lower than that of Cu_2O/MXene (1096 mV dec^{-1}). However, the C_2 and C_3 production for Cu/MXene was much lower than that for Cu_2O/MXene (Figure 4b). These results indicate sluggish reaction kinetics for the C_2 and C_3 hydrocarbon production which require complex multistep reactions including carbon coupling and protonation.[33] Thus, Cu_2O/MXene could effectively enforce the reaction pathway toward multi-carbon production when sufficient time for carbon coupling and protonation was provided during electrochemical CO_2 reduction. In addition, the long-term stability of Cu_2O/MXene at −1.3 V versus RHE up to 48 h was investigated as shown in Figure 4e. After the stability test, Cu_2O NPs stably anchored onto the MXene were observed by HAADF-STEM, and the catalyst was characterized by XRD and XPS, which showed no significant changes (Figure S17, Supporting Information).

To determine the mechanism of how the Cu_2O/MXene affected the selectivity toward C_3 product in CO_2RR, *in-situ* ATR-FTIR spectroscopy was performed and compared with the Cu_2O to reveal the coupling effect of the intermediates such as *CO and *OCCO at the interface. As shown in **Figure 5**a, the peak at 1560–1640 cm^{-1} corresponds to the asymmetric O-C-O stretching peak associated with Cu_2O (Figure 5b) when CO_2 is adsorbed and the C atom is bound to the metallic atom of the catalyst.[34] This O-C-O stretching peak remained after 20 min of CO_2 reduction, indicating that the Cu_2O anchored on the MXene could continuously and strongly bind the CO_2 intermediate.[35] *CHO peak at 1660–1740 cm^{-1} was expected to produce the C_1 pathway toward the formation of CH_4.[36] *COOH peak was found at 1210–1280 cm^{-1} which ultimately led to CO.[37] Notably, *COOH favors the production of CO, which is not a desirable intermediate for HCOOH formation, as has already been proven by several studies.[37a,38] C = C peaks were found at 820–850 cm^{-1} and 940–1030 cm^{-1}, significant evidence of alkene products including C_2H_4.[39] Moreover, peaks for CO dimerization were found at 1470–1530 cm^{-1} and 1390–1460 cm^{-1} which belong to *OCCO and *OCCOH onto the Cu_2O, respectively.[36,40] These CO dimerization intermediates triggered the C_{2+} and C_{3+} pathways, as reported in previous studies for the CO_2RR mechanism to produce C_3 through the C_1-C_2 coupling step.[6d,41] The key feature of this mechanism is the high coverage of the C_2 intermediate, which can be stabilized by a well-designed catalyst morphology and electronic structure.[6d] Here, as the *OCCO and *OCCOH peaks increased with CO_2 electrolysis time, Cu_2O (111) strongly bound CO_2 to C_2 intermediates and provided catalytic sites for a longer time for additional carbon chain elongation and protonation toward C_3H_8, as discussed in the Tafel slopes (Figure 4d; Figure S15, Supporting Information).[41–42] To determine the weak C_3 intermediate peak masked by stronger noise, the first derivative of the ATR-FTIR was processed, which is a common method used for spectral data processing and interpretation (Figure 5c-d).[43] Compared to Cu_2O (CuNP-HT + NH_4OH), an additional peak at ≈690 cm^{-1} for C-CH_2-C peak was found for Cu_2O/MXene, confirming that the C_3 intermediate could generate C_3H_8 (propane), n-C_3H_7OH (n-propanol) or C_2H_3CHO (acrolein) during CO_2 reduction.[44] With Cu_2O, although there are peaks for *CO, *OCCO and *OCCOH, no C-CH_2-C peak at ≈690 cm^{-1} is found, indicating that the C_3 intermediate is not solely found at the Cu_2O catalytic site, as well as additional *CO intermediate adsorption site from the MXene is necessary for C_3 intermediate coupling. Considering that MXene and AT-MXene could not produce C_2 products (Figure S13, Supporting Information), the interface between Cu_2O and MXene in Cu_2O/MXene was the key site for coupling $*C_2$ intermediates and *CO toward C_3 products, where Cu_2O provided adsorption sites for $*C_2$ intermediates and MXene provided adsorption sites for *CO.

As *CO and $*C_2$ bound to couple the carbon chain to C_{3+} products,[3a,7b,45] the gas and liquid products were analyzed by IR and ^{1}H NMR to determine the hydrocarbon products (Figure 5e–f). Several peaks representing hydrocarbons from the CO_2RR were observed. Some unreacted gases, such as CO_2 and H_2O, were also found.[46] Notably, C-C-C skeletal vibration was found at ≈720 cm^{-1}, confirming C_3H_8 production.[47] Through ^{1}H NMR, we found additional liquid hydrocarbon products, including C_2 and C_3 products such as acetaldehyde, acetate, acrolein, and n-propanol.[48] However, only traceable amounts of liquid products were generated during CO_2RR.

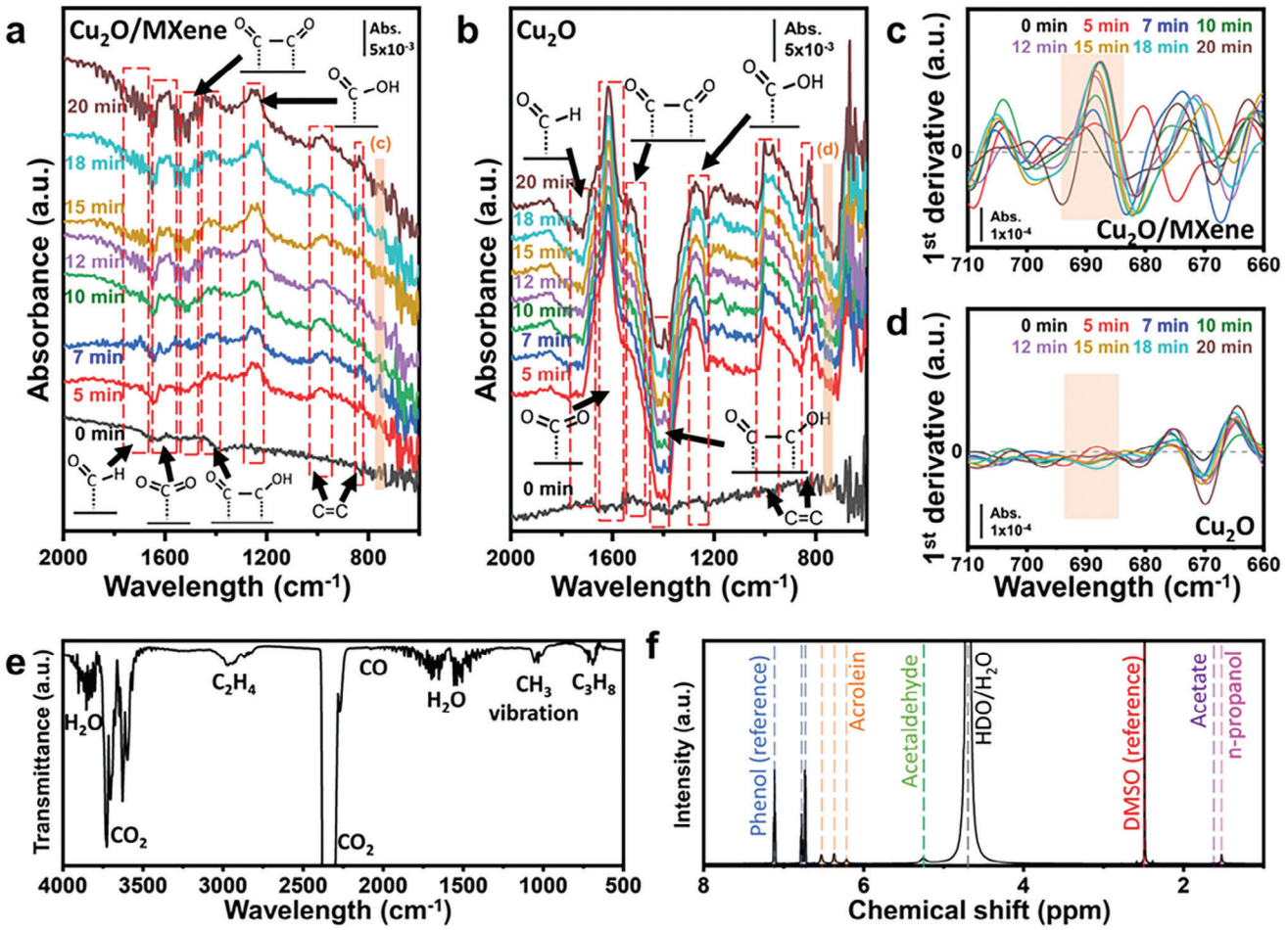

Figure 5. a) and b) ATR-FTIR spectra for Cu_2O/MXene and Cu_2O at varying CO_2RR time. c) and d) 1st derivative of ATR-FTIR spectra for Cu_2O/MXene and Cu_2O in ranges of 660–710 cm^{-1}. e) FT-IR spectra of gas species from Cu_2O/MXene CO_2RR. f) ^1H NMR spectra of Cu_2O/MXene. All the tests were conducted at −1.3 V versus RHE.

2.3. Proposed Mechanism for Electrochemical CO_2 Reduction to C_3H_8

Based on the above mechanistic analysis, we highlighted the key steps and crucial intermediates in C_3H_8 production (Figure S19, Supporting Information). CO_2 was initially adsorbed onto Cu_2O/MXene at both Cu_2O and MXene sites to form *COOH, which underwent further reduction to *CO with H_2O removal.[49] The *CO intermediates on Cu_2O underwent CO dimerization to *OCCO and were further hydrogenated to form *OCCOH.[50] After protonation, *OCCO formed *OCCOH, which is the core step for the formation of C_2 and C_3 hydrocarbons, including C_2H_4, C_2H_6, and C_3H_7OH, following sufficient protonation with electron transfer. Furthermore, the stabilized and protonated *C_2 intermediates on Cu_2O can be coupled with *CO adsorbed on MXene by NH_4OH treatment to form the C_3 intermediate. Additional protonation/electron-transfer steps, including the hydrogenation of the carbon from the intermediate, can transfer this C_3 intermediate to the saturated hydrocarbon, i.e., C_3H_8.[51]

The production of C_3H_8 on Cu_2O/MXene benefits from its nanostructure. The catalyst is composed of Cu_2O with a prevalent Cu_2O (111) facet, which is in favor of binding *C_2 intermediates.[52] MXene also favors CO_2 adsorption because the Gibbs free energy of CO_2 adsorption on MXene is negative, indicating that CO_2 adsorption on MXene is thermodynamically favorable.[53] This hybrid of Cu_2O and MXene couple *C_2-*C_1 intermediates into C_3 products at the interface between Cu_2O and MXene. The NH_4OH treatment modulated the surface group of MXene to -O and -OH, which favors the transfer of protons with low H adsorption energy for the protonation of CO_2RR intermediates.[54] Thus, these synergistic effects on the Cu_2O/MXene structure could increase the C_3H_8 production.

We performed density functional theory (DFT) calculations to gain further insight into the role of MXene on the improved CO_2RR activity for C_3H_8(g) production in the 0D/2D heterostructure composed of Cu_2O (or Cu)-anchored MXene compared to pure Cu_2O and Cu under aqueous condition (**Figure 6**). Preferentially, we investigated the CO_2RR activity of pure Cu_2O(111) and Cu(111) structures through their limiting potential (U_L) evaluated by the free energy diagram (FED) constructed for experimentally observed intermediates in the CO_2RR mechanism depicted in Figure 6a and Figure S19 (Supporting Information)

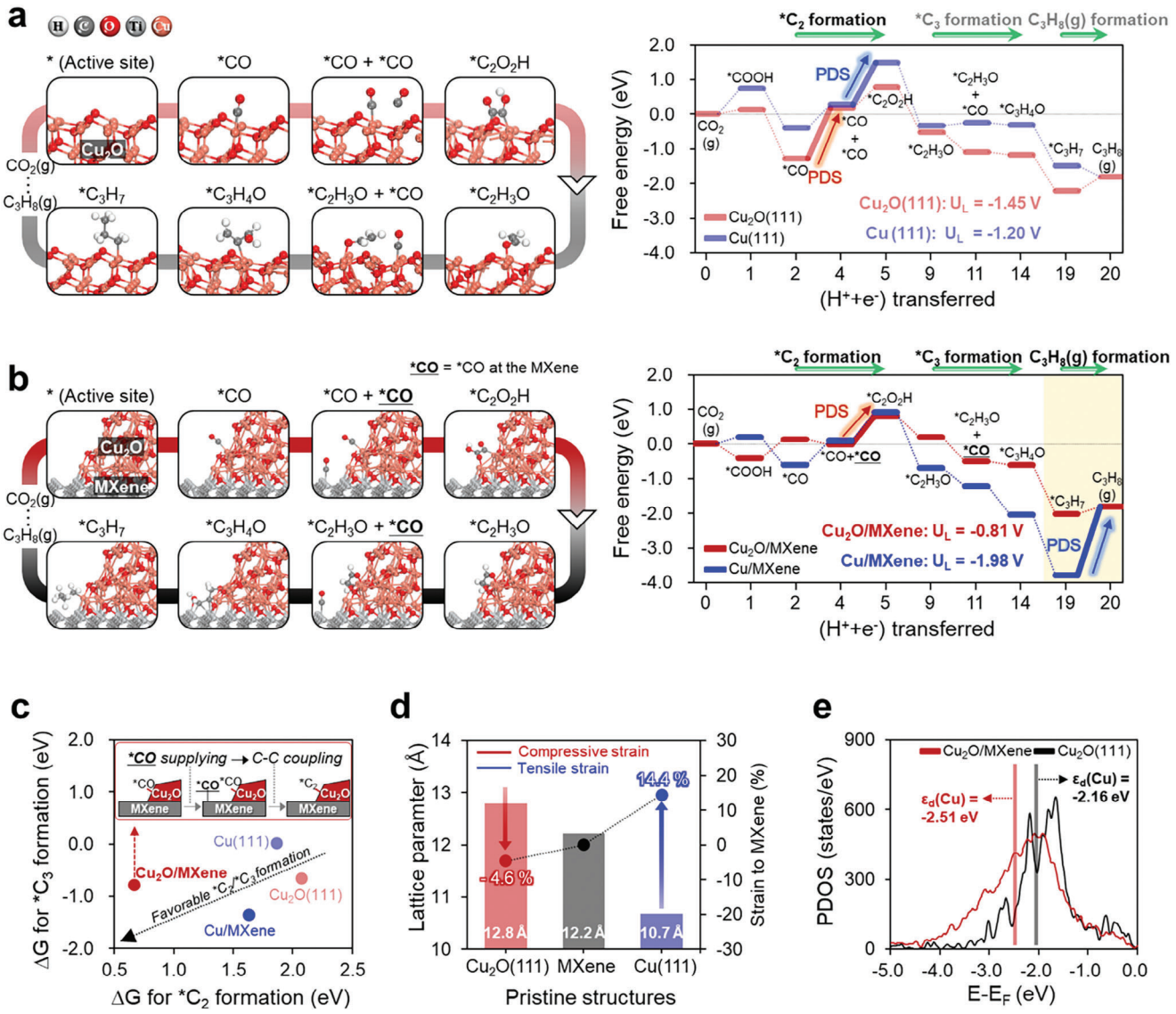

Figure 6. CO_2RR mechanism and calculated free energy diagram (FED) for C_3H_8(g) production in (a) pure Cu_2O(111) structure and b) 0D/2D heterostructure of Cu_2O/MXene. c) Correlation between calculated reaction free energies (DG) for $*C_2$ and $*C_3$ formation through sequential processes of additional *CO supply/C-C coupling in heterostructures of Cu_2O/MXene and Cu/MXene and pure Cu_2O(111) and Cu(111) surfaces. d) Comparison of lattice parameters of pure Cu_2O(111) and Cu(111) compared to MXene structures with respect to compressive or tensile strain. e) Partial density of state (PDOS) of Cu_2O/MXene heterostructure and pure Cu_2O(111) structure for the *d*-band center (ϵ_d) of Cu active sites.

(Details of calculated thermodynamic values for FED are listed in Tables S6 and S7, Supporting Information).[55] The calculated FED in Figure 6a shows that the potential determining steps (PDS) correspond to C_1-C_1 coupling (*CO+*CO → $*C_2O_2H$) and additional *CO supply (*CO → *CO+*CO) steps with U_L values of −1.45 V and −1.20 V at Cu(111) and Cu_2O(111), respectively. The difference in PDS steps for pure Cu_2O(111) and Cu(111) structures can be interpreted by the binding energy of the intermediate. Cu(111) surface has a higher energy barrier in C_1-C_1 coupling for $*C_2O_2H$ formation due to the relatively weak binding energy of intermediates, especially $*C_2O_2H$ and *CO. In contrast, Cu_2O(111) provides a very strong *CO binding at a well-known coordinatively unsaturated Cu site (Cu_{cus}), and additional *CO supply for $*C_2O_2H$ formation cannot be easily achieved because neighboring *CO binding sites are coordinatively saturated Cu site (Cu_{css}) to which *CO cannot stably bind, and instead Cu_{cus} sites are located far apart, as shown in Figure S21 (Supporting Information).[56] Our results imply that $*C_2O_2H$ formation is a thermodynamically unfavorable process in pure Cu_2O(111) and Cu(111) structures, resulting in low $*C_3$ intermediate selectivity. Therefore, MXene can be expected to play a positive role in this $*C_2O_2H$ formation process.

To verify the role of MXene considering the experimentally characterized 0D/2D heterostructures (Figure 1) of Cu_2O/MXene, we first constructed thermodynamically stable 2D/2D heterostructures of Cu_2O and MXene, and then manipulated the Cu_2O interface to expose the MXene surface to become a 0D/2D heterostructure, as shown in Figure 6b.[57] Note

that 2D/2D and 0D/2D heterostructure construction processes and their formation energies are described in Figure S21 and Table S8 (Supporting Information). Using the well-established 0D/2D heterostructures, we constructed FED to clarify the effect of MXene incorporation on the PDS and U_L values (Figure 6b). In the case of Cu_2O/MXene heterostructure, the FED shows improved $*C_2$ intermediate selectivity compared to $Cu_2O(111)$ by lowering U_L value from −1.45 V to −0.81 V. It is also seen that the overall binding energy of intermediates on Cu_2O/MXene is weakened by MXene incorporation, ultimately overcoming the strong *CO binding problem that caused the high energy barrier on the pure $Cu_2O(111)$ surface.[58] In addition, MXene can act as an additional *CO supplier for $*C_2O_2H$ formation through a thermodynamically spontaneous process due to MXene's preference for *CO, as shown in Figure S23 and Table S9 (Supporting Information). In contrast, for the FED of Cu/MXene heterostructure, the higher energy barrier for $*C_2O_2H$ formation at the C_1-C_1 coupling step can be reduced by the overall enhanced binding energy of the intermediate. Subsequently, both Cu_2O/MXene and Cu/MXene heterostructures facilitate the formation of $*C_2O_2H$ and enable further reduction processes as a spontaneous downhill reaction to produce C_3 compounds such as C_3H_8 through $*C_2$-$*C_1$ coupling. Moreover, the correlation analysis between calculated reaction free energies for $*C_2O_2H$ and $*C_3H_4O$ formation through sequential processes of additional *CO supply and C-C coupling in Figure 6c and Table S10 (Supporting Information) clearly shows that the MXene incorporation plays an important role in promoting the formation reactions of $*C_2O_2H$ and $*C_3H_4O$.[59] Therefore, Cu_2O/MXene can proceed CO_2RR to C_3H_8(g) production without specifically high energy barrier. However, Cu/MXene cannot produce the final C_3H_8(g) compound due to the enhanced intermediate binding energy. Especially, the strong binding energy of Cu/MXene for $*C_3H_7$ results in a very high energy barrier for C_3H_8(g) formation, thus increasing the U_L value from −1.20 V to −1.98 V compared to pure Cu(111).

The conflicting behavior of intermediate binding energy can be comprehended by lattice parameter mismatch in the Cu_2O/MXene and Cu/MXene heterostructures, as analyzed in Figure 6d. Cu_2O and Cu in the heterostructure with MXene undergo compressive (−4.6%) and tensile (+14.4%) strain, respectively. Cu in the Cu/MXene heterostructure suffers severe lattice strain, and the extremely large tensile strain on Cu induces strong binding energy of intermediate to stabilize the strained structure through intermediate binding. For Cu_2O in the Cu_2O/MXene heterostructure, the weakened binding energy of the intermediate can be explained by electronic structure modulation, i.e., *d*-band center shift. The binding strength of adsorbents is closely related to the filling of the anti-bonding state near the Fermi level, which is estimated by the *d*-band center (ϵ_d) theory of Hammer and Norskov.[60] The increased filling of the anti-bonding state leads to weak binding energy of adsorbents. The partial density of states (PDOS) analysis of the *d*-orbital of Cu (ϵ_d(Cu)) in Figure 6e reveals that ϵ_d(Cu) of each $Cu_2O(111)$ and Cu_2O/MXene are located at −2.16 eV and −2.51 eV, respectively. Here, the downshifted ϵ_d(Cu) of Cu_2O/MXene position compared to ϵ_d(Cu) of $Cu_2O(111)$ proves that the binding energy of intermediates in Cu_2O/MXene is relatively weak. Consequently, our theoretical calculations clearly show that the incorporation of MXene, especially into the Cu_2O/MXene heterostructure plays a crucial role in the improvement of CO_2RR catalytic activity up to C_3H_8(g) production by regulating the electronic structure and promoting the sequential processes of *CO supplying/C-C coupling.

The intermediates involved in this mechanism are more complicated than those suggested in our study as 3 CO_2 molecules with 20 electrons are required for C_3H_8 production. Nevertheless, the mechanism described in our study offers opportunities for the design of advanced catalysts for the efficient production of C_3H_8, with a pathway for electrochemical CO_2 reduction and protonation of the hydrocarbon intermediates.

3. Conclusion

In summary, we designed $Cu_2O/Ti_3C_2T_x$ MXene, hybridized oxide-derived Cu (Cu_2O) on OH-modulated MXene by NH_4OH treatment and achieved highly active and selective production of C_3H_8 via electrochemical CO_2 reduction reaction in aqueous electrolyte. ATR-FTIR showed that Cu_2O can strongly bind and stably preserve the reaction intermediates on the surface, but additional active sites are required for $*C_2$-$*C_1$ coupling toward C_3 hydrocarbons. Thus, owing to the synergistic effects of Cu_2O and MXene, the interface between Cu_2O and MXene is a key factor for the CO_2 reduction to C_3H_8, where Cu_2O binds $*C_2$ intermediates and MXene binds *CO for C_3 coupling with further efficient protonation for C_3H_8 production. In detailed characterizations, Cu_2O/MXene exhibited a remarkable FE enhancement toward C_3H_8 (≈3.3%), representing a 26-fold increase compared to Cu/MXene without the aid of carbon sources neither on the surface on the catalyst nor the ionomer. DFT calculations also highlight the effective pathway for electrochemical CO_2 reduction and protonation of hydrocarbon intermediates to produce C_3H_8 in the presence of the interface between Cu_2O and MXene. This study not only provides evidence of the reaction process in the selective electrochemical reduction of CO_2 to C_3H_8 but also suggests a rational electrocatalyst design strategy for CO_2RR. This strategy involves multi-carbon coupling as well as protonation to produce high-energy-density products, including hydrogen-rich hydrocarbons.

4. Experimental Section

Synthesis of $Ti_3C_2T_x$ MXene: 2D $Ti_3C_2T_x$ MXene nanosheets were prepared by a typical etching method previously reported with some modifications.[14] Initially, 2.0 g of the MAX powder (Ti_3AlC_2) was added to 20 mL of an aqueous HF solution in a Teflon liner and stirred for 36 h at 50 °C to selectively etch the Al layer from the MAX powder. The obtained suspension was washed several times with deionized water (DI water) via centrifugation to remove the acidic solvent. The precipitated samples were then collected and freeze-dried. After freeze-drying, the 1.0 g of MXene powder was mixed with 12 mL of DMSO and stirred for 18 h at room temperature for intercalation. After intercalation, a tip sonicator was used in an ice-water bath for 4 h for delamination. The resulting solution was centrifuged several times with DI water to remove the remained DMSO. Finally, the obtained MXene was dispersed in DI water and stored in the fridge until use.

Synthesis of Cu Nanoparticles: First, 30 mmol of 1-octadecene, 4 mmol of oleic acid, and 8 mmol of 1,5-pentanediol were mixed and heated at 130 °C for 30 min under an N_2 atmosphere in a two-necked round bottom flask to form solution A. Another bottle of 1 mmol $Cu(acac)_2$ into 5 mmol

oleylamine was heated at 70 °C for 30 min with stirring to form solution B. Subsequently, solution B was injected into solution A and heated at 200 °C for 2 h under stirring. After heating at 200 °C, the obtained solution was then rapidly cooled. To remove organic impurities, the sample was washed and centrifuged several times with hexane and IPA, then freeze-dried. Finally, the products obtained as a powder were denoted as CuNPs.

Synthesis of Cu_2O/MXene: The as-prepared MXene solution was diluted to 1 mg mL^{-1} in DI water and sonicated for 30 min to prevent restacking. The synthesis of Cu_2O/MXene adopted a hydrothermal method. 6 mg of Cu NPs and 4 mmol of ammonia solution (NH_4OH) were added into 25 mL of the MXene solution and kept at 70 °C for 30 min under N_2 to inhibit further oxidation of MXene. For comparison, different mass ratios of CuNPs to MXene were prepared: 2:25, 6:25, and 10:25 wt./wt. (denoted as Cu_2O/MXene 2:25, 6:25, and 10:25, respectively). The mixture was then ultrasonicated at room temperature for 1 h. After sonication, the obtained Cu_2O/MXene sample was washed several times with DI water, centrifuged, and vacuum dried to prevent further oxidation. Cu/MXene was prepared following the same procedure as for Cu_2O/MXene, except for adding 4 mmol of NH_4OH. Additionally, MXene subjected to a hydrothermal process with NH_4OH treatment (AT-MXene) was prepared following the same procedure as for Cu_2O/MXene, except for adding CuNPs.

Electrochemical Measurements: The electrochemical CO_2 reduction reaction (CO_2RR) measurements were conducted by a three-electrode configuration using an electrochemical working station (Gamry Reference 600+). To prepare the working electrode, 2 mg of catalyst was dispersed in 0.5 mL isopropyl alcohol (IPA) with a sonicator. After the sonication, 5 µL of Nafion (5 wt.%) was additionally mixed with the catalyst solution and further ultrasonicated for 30 min to obtain a catalyst ink. The 40 µl of ink was then dropped onto the carbon cloth with a geometric area of 1 cm^2 and dried in the vacuum oven. The carbon cloth was pretreated by soaking it in 3 M HCl for 15 min and then washed several times with DI water and ethanol, followed by N_2 blowing until dry. The Pt plate and Ag/AgCl (3 M NaCl) electrode served as the counter and reference electrodes, respectively. As an electrolyte, CO_2 saturated with 0.1 M $KHCO_3$ (pH = 6.8) was prepared and kept at a CO_2 flow rate of 20 sccm using a mass flow controller during electrochemical CO_2RR measurements. LSV was performed at a scan rate of 5 mV s^{-1}. All potentials were reported with respect to the RHE with the *iR* correction. Electrochemical impedance spectroscopy (EIS) was conducted in the frequency range of 10^5–10^{-1} Hz and amplitude of 5 mV at −1.0 V versus RHE. The electrochemical double-layer capacitance method was used for the electrochemical active surface area (ECSA) measurements, which were extracted from the cyclic voltammograms (CV) at different scan rates (2, 5, 10, 20, and 25 mV s^{-1}) in the non-Faradaic region. Note that all electrochemical data (except stability testing) were repeated more than three times, with error bars representing the standard deviation of the data.

Computational Details: All density functional theory (DFT) calculations were performed with the Vienna Ab initio Simulation Package (VASP 5.4.4).[61] The Projector Augmented Wave (PAW) method[61c,d,62] was employed and exchange-correlation interactions were treated through Perdew-Burke-Ernzerohf (PBE)[63] functional under the generalized gradient approximation (GGA). Monkhorst-Pack k-point meshes of 2 × 4 × 1 and 1 × 4 × 1 were used in each primitive lattice vector of the reciprocal space for geometry optimization of pure Cu_2O(111) and Cu(111) and Cu_2O (or Cu)/MXene heterostructures, respectively with Brillouin zone sampling.[64] And DFT-D3 dispersion correction method was used to reflect the non-bonding interactions correlation in the Cu_2O/MXene system.[63,65] Lattice constants and internal atomic positions were fully optimized using a plane-wave cutoff energy of 500 eV and spin-polarized calculations until the residual forces were less than 0.04 eV $Å^{-1}$. Additional description of the structural information and CO_2RR catalytic activity evaluation is described in the Supporting Information.

Supporting Information

Supporting Information is available from the Wiley Online Library or from the author.

Acknowledgements

This work was supported by the National Research Foundation of Korea (NRF) grant funded by the Korea government (MSIT) (NRF-2022R1A2C1011559, and 2020R1A6A1A03048004). This work was partly supported by the GRRC program of Gyeonggi province [(GRRCKYUNGHEE2023-B01), Development of ultra-fine process materials based on the sub-nanometer class for the next-generation semiconductors]. This work was supported by the Technology Innovation Program (RS-2024-00419747, Development of Materials and Devices Based on Tandem Device to Achieve High Efficiency and Long Lifetime Blue OLEDs for IT Display Applications) funded By the Ministry of Trade, Industry & Energy (MOTIE, Korea). This work is funded by Korea Institute of Science and Technology (KIST) Institutional Program (2E33251). Experiments at PLS-II were supported in part by MSIT and POSTECH.

Conflict of Interest

The authors declare no conflict of interest.

Author Contributions

J.Y.K. and W.T.H. contributed equally to this work. J.Y.K. designed the experiment and methodology and conducted the formal analysis and investigations. W.T.H. performed the data curation, material synthesis, characterization, and investigation. T.K.C.P. performed the methodology, assisted with investigations, and contributed to the initiation of this work. S.C.C. conducted the DFT calculation. B.K. and U.B. assisted with the investigation and methodology. H.-S.O., J.H.K., X.Y., C.-H.C., and J.P. conducted the validations, assisted with the formal analysis, and conducted funding acquisition. S.U.L. supervised the DFT calculation, provided the resources and revised the manuscript. C.-H.C. provided the resources, conducted the investigation and funding acquisition, and assisted with the formal analysis. J.K.K. conceptualized this work, supervised this project, performed project administration, and conducted funding acquisition. All authors contributed to the writing, revising, and editing of this manuscript.

Data Availability Statement

The data that support the findings of this study are available from the corresponding author upon reasonable request.

Keywords

C2-C1 coupling, electrochemical CO2 reduction, in-situ ATR-FTIR, propane production, proton-coupled electron transfer

Received: June 4, 2024
Revised: July 24, 2024
Published online: August 19, 2024

[1] P. De Luna, C. Hahn, D. Higgins, S. A. Jaffer, T. F. Jaramillo, E. H. Sargent, *Science* **2019**, *364*, eeav3506.
[2] a) *Climate Change 2022 – Mitigation of Climate Change*, Cambridge University Press, Cambridge, **2023**; b) J. Y. Kim, D. Kim, Z. J. Li, C. Dariva, Y. K. Cao, N. Ellis, *Energy* **2023**, *263*, 125900.
[3] a) J. H. Du, B. G. Cheng, H. Q. Yuan, Y. Tao, Y. Chen, M. Ming, Z. J. Han, R. Eisenberg, *Angew. Chem. Int. Ed.* **2023**, *62*, e202211804; b) Y. Q. Liu, Z. Y. Guo, Z. Y. Qiu, W. W. Wang, H. P. Lin, X. Zhao, J. S. Dang, *ACS Appl. Mater. Interfaces* **2022**, *14*, 46657.

[4] M. Esmaeilirad, Z. Jiang, A. M. Harzandi, A. Kondori, M. Tamadoni Saray, C. U. Segre, R. Shahbazian-Yassar, A. M. Rappe, M. Asadi, *Nat. Energy* **2023**, *8*, 891.
[5] A. Fortunati, F. Risplendi, M. Re Fiorentin, G. Cicero, E. Parisi, M. Castellino, E. Simone, B. Iliev, T. J. S. Schubert, N. Russo, S. Hernandez, *Commun. Chem.* **2023**, *6*, 84.
[6] a) Q. Zhu, X. Sun, D. Yang, J. Ma, X. Kang, L. Zheng, J. Zhang, Z. Wu, B. Han, *Nat. Commun.* **2019**, *10*, 3851; b) Y. H. Wang, J. L. Liu, G. F. Zheng, *Adv. Mater.* **2021**, *33*, 2005798; c) A. R. Woldu, Z. L. Huang, P. X. Zhao, L. S. Hu, D. Astruc, *Coord. Chem. Rev.* **2022**, *454*, 214340; d) Y. Zheng, A. Vasileff, X. L. Zhou, Y. Jiao, M. Jaroniec, S. Z. Qiao, *J. Am. Chem. Soc.* **2019**, *141*, 7646.
[7] a) W. Y. Zhi, Y. T. Liu, S. L. Shan, C. J. Jiang, H. Wang, J. X. Lu, *J CO2 Util* **2021**, *50*, 101594; b) M. M. Abdelnaby, K. L. Liu, K. Hassanein, Z. Y. Yin, *Chem. Nano. Mat.* **2021**, *7*, 969; c) H. J. Ren, M. Kovalev, Z. Y. Weng, M. Z. Muhamad, H. Y. Ma, Y. Sheng, L. B. Sun, J. J. Wang, S. Rihm, W. F. Yang, A. A. Lapkin, J. W. Ager, *Nat. Catal.* **2022**, *5*, 1169.
[8] a) L. R. L. Ting, R. García-Muelas, A. J. Martín, F. L. P. Veenstra, S. T. J. Chen, Y. J. Peng, E. Y. X. Per, S. Pablo-García, N. López, J. Pérez-Ramírez, B. S. Yeo, *Angew. Chem. Int. Ed.* **2020**, *59*, 21072; b) Z. D. Li, N. H. Attanayake, J. L. Blackburn, E. M. Miller, *Energy Environ. Sci.* **2021**, *14*, 1696; c) R. Kortlever, R. Kortlever, I. Peters, I. Peters, C. Balemans, C. Balemans, R. Kas, R. Kas, Y. Kwon, Y. Kwon, G. Mul, G. Mul, M. T. M. Koper, M. T. M. Koper, *Chem. Commun.* **2016**, *52*, 10229.
[9] J. C. Zhang, W. Z. Cai, F. X. Hu, H. B. Yang, B. Liu, *Chem. Sci.* **2021**, *12*, 6800.
[10] C. J. Lu, L. Yang, B. Z. Yan, L. B. Sun, P. G. Zhang, W. Zhang, Z. M. Sun, *Adv. Funct. Mater.* **2020**, *30*, 2000852.
[11] H. T. Chen, A. D. Handoko, J. W. Xiao, X. Feng, Y. C. Fan, T. S. Wang, D. Legut, Z. W. Seh, Q. F. Zhang, *ACS Appl. Mater. Interfaces* **2019**, *11*, 36571.
[12] D. Y. Zhao, R. Z. Zhao, S. H. Dong, X. G. Miao, Z. W. Zhang, C. X. Wang, L. W. Yin, *Energy Environ. Sci.* **2019**, *12*, 2422.
[13] W. L. Fu, Z. Liu, T. Y. Wang, J. S. Liang, S. Duan, L. F. Xie, J. T. Han, Q. Li, *ACS Sustain. Chem. Eng.* **2020**, *8*, 15223.
[14] D. N. Nguyen, G. S. Gund, M. G. Jung, S. H. Roh, J. Park, J. K. Kim, H. S. Park, *ACS Nano* **2020**, *14*, 17615.
[15] a) T. A. Le, Q. V. Bui, N. Q. Tran, Y. Cho, Y. Hong, Y. Kawazoe, H. Lee, *ACS Sustain. Chem. Eng.* **2019**, *7*, 16879; b) X. L. Kong, Z. B. Peng, R. Jiang, P. P. Jia, J. Feng, P. P. Yang, Q. Q. Chi, W. Ye, F. C. Xu, P. Gao, *ACS Appl. Nano Mater.* **2020**, *3*, 1373; c) Q. Zhao, C. Zhang, R. M. Hu, Z. G. Du, J. N. Gu, Y. L. S. Cui, X. Chen, W. J. Xu, Z. J. Cheng, S. M. Li, B. Li, Y. F. Liu, W. H. Chen, C. T. Liu, J. X. Shang, L. Song, S. B. Yang, *ACS Nano* **2021**, *15*, 4927.
[16] M. Naguib, O. Mashtalir, J. Carle, V. Presser, J. Lu, L. Hultman, Y. Gogotsi, M. W. Barsoum, *ACS Nano* **2012**, *6*, 1322.
[17] a) K. A. S. Raj, N. Barman, S. Radhakrishnan, R. Thapa, C. S. Rout, *J. Mater. Chem. A* **2022**, *10*, 23590; b) X. Wang, H. Li, H. Li, S. Lin, W. Ding, X. G. Zhu, Z. G. Sheng, H. Wang, X. B. Zhu, Y. P. Sun, *Adv. Funct. Mater.* **2020**, *30*, 1910302.
[18] Q. Xue, H. J. Zhang, M. S. Zhu, Z. X. Pei, H. F. Li, Z. F. Wang, Y. Huang, Y. Huang, Q. H. Deng, J. Zhou, S. Y. Du, Q. Huang, C. Y. Zhi, *Adv. Mater.* **2017**, *29*, 1604847.
[19] M. A. Raza, F. Li, M. D. Que, L. L. Zhu, X. Chen, *Adv. Funct. Mater.* **2021**, *2*, 7187.
[20] Y. Xiao, C. Men, B. X. Chu, Z. Z. Qin, H. B. Ji, J. H. Chen, T. M. Su, *Chem. Eng. J.* **2022**, *446*, 137028.
[21] Y. Wang, H. Dou, J. Wang, B. Ding, Y. L. Xu, Z. Chang, X. D. Hao, *J. Power Sources* **2016**, *327*, 221.
[22] H. H. Bao, Y. Qiu, X. Y. Peng, J. A. Wang, Y. Y. Mi, S. Z. Zhao, X. J. Liu, Y. F. Liu, R. Cao, L. C. Zhuo, J. Q. Ren, J. Q. Sun, J. Luo, X. P. Sun, *Nat. Commun.* **2021**, *12*, 238.
[23] Y. Cao, Q. H. Deng, Z. D. Liu, D. Y. Shen, T. Wang, Q. Huang, S. Y. Du, N. Jiang, C. T. Lin, J. H. Yu, *RSC Adv.* **2017**, *7*, 20494.
[24] a) D. N. Nguyen, T. K. C. Phu, J. Kim, W. T. Hong, J. S. Kim, S. H. Roh, H. S. Park, C. H. Chung, W. S. Choe, H. Shin, J. Y. Lee, J. K. Kim, *Small* **2022**, *18*, 2204797; b) Y. K. Zhang, H. L. Jiang, Y. X. Lin, H. J. Liu, Q. He, C. Q. Wu, T. Duan, L. Song, *Adv. Mater. Interfaces* **2018**, *5*, 1800392.
[25] a) T. T. Hou, Q. Q. Luo, Q. Li, H. L. Zu, P. X. Cui, S. W. Chen, Y. Lin, J. J. Chen, X. S. Zheng, W. K. Zhu, S. Q. Liang, J. L. Yang, L. B. Wang, *Nat. Commun.* **2020**, *11*, 4251; b) H. Y. Zhou, S. J. Han, H. D. Lee, D. Z. Zhang, M. Anayee, S. H. Jo, Y. Gogotsi, T. W. Lee, *Adv. Mater.* **2022**, *34*, 2206377; c) T. Schultz, N. C. Frey, K. Hantanasirisakul, S. Park, S. J. May, V. B. Shenoy, Y. Gogotsi, N. Koch, *Chem. Mater.* **2019**, *31*, 6590; d) M. Benchakar, L. Loupias, C. Garnero, T. Bilyk, C. Morais, C. Canaff, N. Guignard, S. Morisset, H. Pazniak, S. Hurand, P. Chartier, J. Pacaud, V. Mauchamp, M. W. Barsoum, A. Habrioux, S. Célérier, *Appl. Surf. Sci.* **2020**, *530*, 147209.
[26] a) T. Kobayashi, Y. Y. L. Sun, K. Prenger, D. E. Jiang, M. Naguib, M. Pruski, *J. Phys. Chem. C* **2020**, *124*, 13649; b) Y. Zhou, Y. H. Wang, Y. J. Wang, X. Li, *Anal. Chem.* **2020**, *92*, 16033; c) W. Y. Chen, X. F. Jiang, S. N. Lai, D. Peroulis, L. Stanciu, *Nat. Commun.* **2020**, *11*, 1302.
[27] H. W. Wang, M. Naguib, K. Page, D. J. Wesolowski, Y. Gogotsi, *Chem. Mater.* **2016**, *28*, 349.
[28] S. L. Chu, C. Kang, W. Park, Y. Han, S. Hong, L. D. Hao, H. Zhang, T. W. B. Lo, A. W. Robertson, Y. S. Jung, B. X. Han, Z. Y. Sun, *SmartMat* **2022**, *3*, 194.
[29] A. Sarycheva, Y. Gogotsi, *Chem. Mater.* **2020**, *32*, 3480.
[30] a) H. Maaoui, S. K. Singh, F. Teodorescu, Y. Coffinier, A. Barras, R. Chtourou, S. Kurungot, S. Szunerits, R. Boukherroub, *Electrochim. Acta* **2017**, *224*, 346; b) Y. W. Jiang, X. Y. Wang, D. L. Duan, C. H. He, J. Ma, W. Q. Zhang, H. J. Liu, R. Long, Z. B. Li, T. T. Kong, X. J. Loh, L. Song, E. N. Ye, Y. J. Xiong, *Adv. Sci.* **2022**, *9*, 2105292.
[31] a) Y. Yang, A. B. He, H. Li, Q. Zou, Z. H. Liu, C. Y. Tao, J. Du, *ACS Catal.* **2022**, *12*, 12942. b) J. H. Li, K. Q. Xu, F. M. Liu, Y. Z. Li, Y. F. Hu, X. J. Chen, H. Wang, W. C. Xu, Y. X. Ni, G. Y. Ding, T. T. Zhao, M. Yu, W. Xie, F. Y. Cheng, *Adv. Mater.* **2023**, *35*, 2301127; c) J. Timoshenko, A. Bergmann, C. Rettenmaier, A. Herzog, R. M. Arán-Ais, H. S. Jeon, F. T. Haase, U. Hejral, P. Grosse, S. Kühl, E. M. Davis, J. Tian, O. Magnussen, B. R. Cuenya, *Nat. Catal.* **2022**, *5*, 259.
[32] C. L. Yan, W. Luo, H. M. Yuan, G. Y. Liu, R. Hao, N. Qin, Z. Q. Wang, K. Liu, Z. Y. Wang, D. H. Cui, Z. F. Hu, Y. C. Lan, Z. G. Lu, *Appl. Catal. B* **2022**, *308*, 121191.
[33] T. Kim, A. Kargar, Y. Q. Luo, R. Mohammed, E. Martinez-Loran, A. Ganapathi, P. Shah, D. P. Fenning, *ACS Appl. Energy Mater.* **2018**, *1*, 1965.
[34] a) D. F. Gao, H. Zhou, F. Cai, D. N. Wang, Y. F. Hu, B. Jiang, W. B. Cai, X. Q. Chen, R. Si, F. Yang, S. Miao, J. G. Wang, G. X. Wang, X. H. Bao, *Nano Res.* **2017**, *10*, 2181; b) K. Ogura, *J CO2 Util* **2013**, *1*, 43; c) J. E. Lee, A. Yamaguchi, H. Ooka, T. Kazami, M. Miyauchi, N. Kitadai, R. Nakamura, *Chem. Comm.* **2021**, *57*, 3267.
[35] a) V. C. Holmberg, B. A. Korgel, *Chem. Mater.* **2010**, *22*, 3698; b) J. Wood, M. J. Alldrick, J. M. Winterbottom, E. H. Stitt, S. Bailey, *Catal. Today* **2007**, *128*, 52.
[36] Y. Kim, S. Park, S. J. Shin, W. Choi, B. K. Min, H. Kim, W. Kim, Y. J. Hwang, *Energ Environ. Sci.* **2020**, *13*, 4301.
[37] a) N. Podrojková, V. Sans, A. Orinak, R. Orinaková, *ChemCatChem* **2020**, *12*, 1802; b) M. Van den Bossche, C. Rose-Petruck, H. Jónsson, *J. Phys. Chem. C* **2021**, *125*, 13802; c) T. Cheng, H. Xiao, W. A. Goddard, *J. Am. Chem. Soc.* **2016**, *138*, 13802.
[38] a) Y. Katayama, F. Nattino, L. Giordano, J. Hwang, R. R. Rao, O. Andreussi, N. Marzari, Y. Shao-Horn, *J. Phys. Chem. C* **2019**, *123*, 5951; b) D. L. T. Nguyen, Y. Kim, Y. J. Hwang, D. H. Won, *Carbon Energy* **2020**, *2*, 72.

[39] B. N. Choi, J. Y. Seo, Z. An, P. J. Yoo, C. H. Chung, *Chem. Eng. J.* **2022**, *430*, 132807.
[40] X. Zhi, Y. Jiao, Y. Zheng, A. Vasileff, S. Z. Qiao, *Nano Energy* **2020**, *71*, 104601.
[41] J. Gao, A. Bahmanpour, O. Kröcher, S. M. Zakeeruddin, D. Ren, M. Grätzel, *Nat. Chem.* **2023**, *15*, 705.
[42] J. J. Ternero-Hidalgo, M. Daturi, G. Clet, P. Bazin, M. A. Bañares, R. Portela, M. O. Guerrero-Pérez, J. Rodríguez-Mirasol, T. Cordero, *Catal. Today* **2022**, *387*, 197.
[43] C. Chen, F. F. Chen, B. Yang, K. Zhang, X. Y. Lv, C. Chen, *Spectrochim. Acta A: Mol. Biomol. Spectrosc.* **2022**, *269*, 120684.
[44] G. Socrates, *Infrared and Raman Characteristic Group Frequencies: Tables and Charts*, 3rd ed., John Wiley & Sons, New York, **2004**.
[45] M. Rahaman, K. Kiran, I. Z. Montiel, V. Grozovski, A. Dutta, P. Broekmann, *Green Chem.* **2020**, *22*, 6497.
[46] a) M. E. G. Winkler, R. H. Gonçalves, A. F. Rubira, *ACS Omega* **2022**, *7*, 45067; b) R. Schwan, M. Kaufmann, D. Leicht, G. Schwaab, M. Havenith, *Phys. Chem. Chem. Phys.* **2016**, *18*, 24063.
[47] a) A. Moosakhani, P. Parvin, A. Reyhani, S. Z. Mortazavi, *Phys. Plasmas* **2017**, *24*, 13505; b) J. J. Harrison, P. F. Bernath, *J. Quant. Spectrosc. Radiat. Transf.* **2010**, *111*, 1282.
[48] a) K. P. Kuhl, E. R. Cave, D. N. Abram, T. F. Jaramillo, *Energ. Environ. Sci.* **2012**, *5*, 7050; b) S. D. Rihm, M. K. Kovalev, A. A. Lapkin, J. W. Ager, M. Kraft, *Energ. Environ. Sci.* **2023**, *16*, 1697.
[49] A. Vasileff, Y. P. Zhu, X. Zhi, Y. Q. Zhao, L. Ge, H. M. Chen, Y. Zheng, S. Z. Qiao, *Angew. Chem. Int. Ed.* **2020**, *59*, 19649.
[50] S. Nitopi, E. Bertheussen, S. B. Scott, X. Y. Liu, A. K. Engstfeld, S. Horch, B. Seger, I. E. L. Stephens, K. Chan, C. Hahn, J. K. Norskov, T. F. Jaramillo, I. Chorkendorff, *Chem. Rev.* **2019**, *119*, 7610.
[51] a) A. D. Handoko, F. X. Wei, Jenndy, B. S. Y., Z. W. Seh, *Nat. Catal.* **2018**, *1*, 922; b) L. Fan, C. Xia, F. Q. Yang, J. Wang, H. T. Wang, Y. Y. Lu, *Sci. Adv.* **2020**, *6*, eaay3111.
[52] Y. G. Gao, Q. Wu, X. Z. Liang, Z. Y. Wang, Z. K. Zheng, P. Wang, Y. Y. Liu, Y. Dai, M. H. Whangbo, B. B. Huang, *Adv. Sci.* **2020**, *7*, 1902820.
[53] Z. L. Guo, Y. Li, B. S. Sa, Y. Fang, J. Lin, Y. Huang, C. C. Tang, J. Zhou, N. H. Miao, Z. M. Sun, *Appl. Surf. Sci.* **2020**, *521*, 146.
[54] T. P. Nguyen, D. M. T. Nguyen, D. L. Tran, H. K. Le, D. V. N. Vo, S. S. Lam, R. S. Varma, M. Shokouhimehr, C. C. Nguyen, Q. V. Le, *Mol. Catal.* **2020**, *486*, 110850.
[55] a) J. K. Norskov, J. Rossmeisl, A. Logadottir, L. Lindqvist, J. R. Kitchin, T. Bligaard, H. Jónsson, *J. Phys. Chem. B* **2004**, *108*, 17886; b) I. C. Man, H. Y. Su, F. Calle-Vallejo, H. A. Hansen, J. I. Martínez, N. G. Inoglu, J. Kitchin, T. F. Jaramillo, J. K. Norskov, J. Rossmeisl, *ChemCatChem* **2011**, *3*, 1159.
[56] L. N. Wu, Z. Y. Tian, W. Qin, *Molecules* **2022**, *27*, 6748.
[57] a) S. S. Shinde, J. Y. Jung, N. K. Wagh, C. H. Lee, D. H. Kim, S. H. Kim, S. U. Lee, J. H. Lee, *Nat. Energy* **2021**, *6*, 592; b) A. A. Ahmed, C. H. Lee, A. Ansari, S. M. Pawar, J. Han, S. Park, G. Shin, S. Yeon, S. Cho, J. Seol, S. U. Lee, H. Kim, H. Im, *Appl. Surf. Sci.* **2022**, *592*, 153196; c) N. K. Wagh, D. H. Kim, C. H. Lee, S. H. Kim, H. D. Um, J. S. I. Kwon, S. S. Shinde, S. U. Lee, J. H. Lee, *Nanoscale Horiz.* **2023**, *8*, 921; d) S. S. Shinde, N. K. Wagh, C. H. Lee, D. H. Kim, S. H. Kim, H. D. Um, S. U. Lee, J. H. Lee, *Adv. Mater.* **2023**, *35*, 2303509; e) J. Yang, S. C. Cho, S. Lee, J. W. Yoon, W. H. Jeong, H. C. Song, J. T. Oh, S. G. Lim, S. Y. Bae, B. R. Lee, M. Ahmadi, E. H. Sargent, W. Yi, S. U. Lee, H. Choi, *ACS Nano* **2022**, *16*, 1649.
[58] a) N. K. Wagh, S. S. Shinde, C. H. Lee, S.-H. Kim, D.-H. Kim, H.-D. Um, S. U. Lee, J.-H. Lee, *Nanomicro Lett.* **2022**, *14*, 190; b) H. Jin, H. S. Kim, C. H. Lee, Y. Hong, J. Choi, H. Baik, S. U. Lee, S. J. Yoo, K. Lee, H. S. Park, *ACS Catal.* **2022**, *12*, 13638.
[59] a) T. C. Kuo, J. W. Chou, M. H. Shen, Z. S. Hong, T. H. Chao, Q. Lu, M. J. Cheng, *J. Phys. Chem. C* **2021**, *125*, 2464; b) S. Pablo-García, F. L. P. Veenstra, L. R. L. Ting, R. García-Muelas, F. Dattila, A. J. Martín, B. S. Yeo, J. Pérez-Ramírez, N. López, *Catal. Sci. Technol.* **2022**, *12*, 409; c) X. Wang, Z. Y. Wang, T. T. Zhuang, C. T. Dinh, J. Li, D. H. Nam, F. W. Li, C. W. Huang, C. S. Tan, Z. T. Chen, M. F. Chi, C. M. Gabardo, A. Seifitokaldani, P. Todorovic, A. Proppe, Y. J. Pang, A. R. Kirmani, Y. H. Wang, A. H. Ip, L. J. Richter, B. Scheffel, A. N. Xu, S. C. Lo, S. O. Kelley, D. Sinton, E. H. Sargent, *Nat. Commun.* **2019**, *10*, 5186; d) X. Wang, P. F. Ou, A. Ozden, S. F. Hung, J. Tam, C. M. Gabardo, J. Y. Howe, J. Sisler, K. Bertens, F. P. G. de Arquer, R. K. Miao, C. P. O'Brien, Z. Y. Wang, J. Abed, A. S. Rasouli, M. J. Sun, A. H. Ip, D. Sinton, E. H. Sargent, *Nat. Energy* **2022**, *7*, 170.
[60] B. Hammer, J. K. Norskov, *Nature* **1995**, *376*, 238.
[61] a) G. Kresse, J. Hafner, *Phys. Rev. B* **1993**, *48*, 13115; b) G. Kresse, J. Hafner, *Phys. Rev. B* **1994**, *49*, 14251; c) G. Kresse, J. Furthmuller, *Comput. Mater. Sci.* **1996**, *6*, 15; d) G. Kresse, J. Furthmüller, *Phys. Rev. B* **1996**, *54*, 11169.
[62] a) P. E. Blochl, *Phys. Rev. B* **1994**, *50*, 17953; b) G. Kresse, D. Joubert, *Phys. Rev. B* **1999**, *59*, 1758.
[63] J. P. Perdew, K. Burke, M. Ernzerhof, *Phys. Rev. Lett.* **1996**, *77*, 3865.
[64] H. Monkhorst, J. Pack, *Phys. Rev. B* **1976**, *13*, 5188.
[65] S. Grimme, J. Antony, S. Ehrlich, H. Krieg, *J. Chem. Phys.* **2010**, *132*, 154104.